A Label Similarity Probability Filter for Hyperspectral Image Postclassification

Weiwei Sun, *Senior Member, IEEE*, Gang Yang, *Member, IEEE*, Kai Ren, Jiangtao Peng, *Senior Member, IEEE*, Chiru Ge, *Student Member, IEEE*, Xiangchao Meng, *Member, IEEE*, and Qian Du, *Fellow, IEEE*

***Abstract*—This article presents a label similarity probability filter (LSPF) to make hyperspectral image postclassification. The LSPF is inspired by the first law of geography and proposes a class label probability function to quantify the probability of both centered and its neighboring pixels belonging to the same class. It first classifies the hyperspectral data using the regular support vector machine classifier. Then, it binarizes the posterior classification result to obtain the binary label maps of each class. After that, it traverses all spatial windows centered by each pixel and calculates the cumulative probability of all pixels in each class. Finally, the cumulative probabilities are used to make reclassification to obtain the refined classification map. The experiments on Indian Pines, Pavia University, and ZY1-02D Yellow River Estuary data show that LSPF greatly improves the classification accuracy of spectral signatures and outperforms other state-of-the-art spectral–spatial methods.**

***Index Terms*—Hyperspectral, label similarity probability filter (LSPF), postclassification, spectral–spatial methods.**

I. Introduction

Hyperspectral imaging sensor, as an advanced earth-observation technique, can simultaneously capture hundreds of narrow spectral bands that often range from visible to shortwave infrared wavelength [1], [2]. Using slight spectral divergences of different materials, the collected hyperspectral images can be applied to recognize diverse ground objects [3], [4]. However, affected by local geographical, environmental factors (e.g., topography, incident illumination, and atmospheric effects), spectral signatures of the same ground objects have clear variations across different spatial locations [5], which brings out a big challenge for the accurate classification of hyperspectral data. Fortunately, the imagery property of hyperspectral data contains enough spatial information and has been proven to benefit the classification [6], [7]. Therefore, it has a great future to combine the spatial and spectral information to boost the pixelwise classification accuracy [8], [9].

During the past two decades, many spectral–spatial methods have been presented, which can be grouped into three main categories [10], [11], i.e., preprocessing-based [12], integrated [13], and postprocessing-based methods [14], according to the step where spatial information is plugged into the classifier. Preprocessing-based methods extract spatial features from an original image and then push them into a standard classifier [15]. The representative methods include three-dimensional (3-D) Gabor filters [16] that extract suitable magnitude features, extend morphology profiles [17] that make mathematical morphological operations with structural elements in various sizes, attribute profiles and extinct profiles that extract attribute morphological characteristics [18], [19], and differential morphology profiles [20] that depict the response of image structures related to different scales and sizes of the structural elements. It is clearly specified that the extracted spatial features highly determine the behaviors of preprocessing-based methods [21]. The integrated methods define a spatial descriptor by exploring the correlation among nearby pixels within the same spatial neighborhood and combine it with spectral signatures to formulate a spectral–spatial classifier [22]. For example, a support vector machine (SVM) with composite kernels (SVM-CK) [23] incorporates both spectral and local spatial information into composite kernels to boost the classification performance of SVM. The sparse representation classifier integrates local spatial information by exploring the dependencies among neighboring pixels within the same spatial window [24]. However, the behaviors of integrated methods are sensitive to parameter settings. A too small or too large spatial neighborhood would degrade the characterization accuracy of spatial information and deteriorate the classification result [25]. Postprocessing-based methods implement a defined spatial operator or filter to regularize *a posteriori* or preobtained classification map [26]. For example, an adaptive

Manuscript received May 16, 2021; revised June 8, 2021; accepted June 27, 2021. Date of publication July 5, 2021; date of current version July 20, 2021. This work was supported in part by National Natural Science Foundation under Grant 41971296, Grant 41671342, Grant 41801256, Grant U1609203, and Grant 61871177, in part by the Zhejiang Provincial Natural Science Foundation of China under Grant LR19D010001 and Grant LQ18D010001, and in part by K. C. Wong Magna Fund in Ningbo University. *(Corresponding author: Gang Yang.)*

Weiwei Sun, Gang Yang, and Kai Ren are with the Department of Geography and Spatial Information Techniques, Ningbo University, Ningbo 315000, China (e-mail: sunweiwei@nbu.edu.cn; yanggang@nbu.edu.cn; 15158346549@163.com).

Jiangtao Peng is with the Hubei Key Laboratory of Applied Mathematics, Faculty of Mathematics and Statistics, Hubei University, Wuhan 430062, China (e-mail: pengjt1982@126.com).

Chiru Ge is with the School of Information Science and Engineering, Shandong Normal University, Jinan 250014, China (e-mail: gechirumsu@gmail.com).

Xiangchao Meng is with the Faculty of Electrical Engineering and Computer Science, Ningbo University, Ningbo 315000, China (e-mail: mengxiangchaoabc@gmail.com).

Qian Du is with the Department of Electrical and Computer Engineering, Mississippi State University, Starkville, MS 39762 USA (e-mail: du@ece.msstate.edu).

Digital Object Identifier 10.1109/JSTARS.2021.3094197

weighted graph was used in a regression model to regularize preobtained class-belonging probabilities from a collaborative representation classifier [27]. The guiding images employ a guider filter and bilateral filter (BF) to depict homogeneity disruption of class labels to guide an edge-preserving classification from SVM [28]. Markov random field assumes that the neighboring pixels take the same class label with high probability and was used to regularize *a posteriori* classification map from multinomial logistic regression [29].

In this article, we present a simple but effective filter named label similarity probability filter (LSPF) to improve *a posteriori* classification map on hyperspectral data. The LSPF is inspired by the first law of geography and assumes that two spatially closer pixels within a neighborhood have a higher probability of taking the same class labels when compared against other pixels that are further away. It defines the label similarity probability (LSP) to quantify the correlations between the center pixel and its neighbors within the same spatial window. Furthermore, it filters the binary label maps using the LSPF to calculate the cumulative probabilities of each pixel in all classes to refine the preobtained class label.

When compared against other current postprocessing methods, our approaches favor three main scientific contributions.

1) Our LSPF has a different idea from current postprocessing methods. The LSPF estimates the label probability of all pixels in all the classes by using the spatial correlations with surrounding pixels and then implements the probability data into the classifier to refine the preobtained classification map.
2) Our LSP is the first explicit operator to adaptively depict the class label similarity between the center pixel and its surrounding pixels. The LSP improves from the Gaussian distribution function but is different from and could automatically consider different spatial heterogeneity of ground objects in the local windows of hyperspectral data.
3) Our LSPF is easy to implement and has good performance in refining the pixelwise classification map.

The rest of this article is arranged as follows. Section II presents the methodology of our LSPF. Section III describes the experimental results on three popular hyperspectral data. Finally, Section IV gives the conclusion of this article.

II. Label Similarity Probability Filter

A. Our Motivation

Due to the spectral similarity of the ground objects, the misclassification and omission of the labels usually cause serious salt and pepper noisy labels, which has a serious impact on hyperspectral mapping [30]. Fortunately, postprocessing methods can improve the accuracy of hyperspectral classification by regularizing the prior labels [31]. However, the current postprocessing methods improve the visualization results and accuracy of the classified images, there are still many false labels [32]. The reason is that these methods are not considered the spatial correlation between the neighboring pixels, and more parameters also make these methods less robust [33], [34]. Therefore, an adaptive prior label probability statistical method is meaningful for the refinement of prior labels to obtain the accurate classification result [35].

When having the preclassification result from regular classifiers, such as SVM, the classification map can be transformed into a series of binary classification maps (i.e., a pixel that belongs to the class c will have 1, otherwise have 0). The first law of geography tells us that all pixels in the image scene are spatially correlated to others else, and the closer pixels are to one another, the more they are correlated. Accordingly, in some sense, within a certain spatial window (e.g., 5 × 5, 7 × 7, or others), the pixels that are closer to the center pixel can be regarded to have a higher probability of taking the same class label with it when compared with those that are further away. In detail, within a certain spatial window of ground objects on the hyperspectral data, the surrounding pixels are closer to the center pixel; they are more likely to belong to the same classes of ground objects, i.e., have a larger LSP with the center pixel on the same class.

We assume that spatial correlations between the center pixel and its surrounding ones follow the Gaussian probability distribution. And then, the 2-D Gaussian function is implemented to depict the LSPs in the local spatial window size. If the center pixel has preobtained class label in class i, the LSP of the center pixel on class i is 1, which is consistent with the reality. For the surrounding pixels, the LSP on the ith class decreases with the spatial distance from the center pixel. For each class, it is easy to find that the LSFs of surrounding pixels are correlated with two main factors: the spatial window size and the degradation gradient with the changing distance. The spatial window size determines the number of pixels that are correlated with the center pixel. The degradation intensity of LSF is determined by the spatial heterogeneity of ground objects within the same spatial window. That is, a stronger spatial heterogeneity brings about a larger degradation intensity and vice-versa. Using the LSF and the preobtained binary classification map on each class, we can obtain the accumulative probabilities of all the pixels on all classes, where the location of a bigger entry indicates that the pixel belongs to the corresponding class with a larger possibility. Furthermore, using the regular SVM classifier, we reclassified the accumulative probability data of all pixels into different classes and obtained the refined classification map.

B. Formulating the LSP for Each Class

The first law of geography indicates that the LSP decreases with the increasing spatial distance between the center pixel and its neighboring. Considering the simplicity and effectiveness of 2-D Gaussian distribution in a realistic world, we implement the exponential function to model the LSP in the local spatial window. The formulation is defined as

$$g\left(x, y\right) = e^{-\left(x^2+y^2\right)/2\sigma^2} \tag{1}$$

where e is the natural constant, $g(x, y)$ is the LSP between the center pixel and its neighboring pixels in the same spatial window, with that of the center pixel as 1. Here, (x, y) is the local image coordinates against the center pixel determined by the spatial window size d, and σ is the standard deviation that

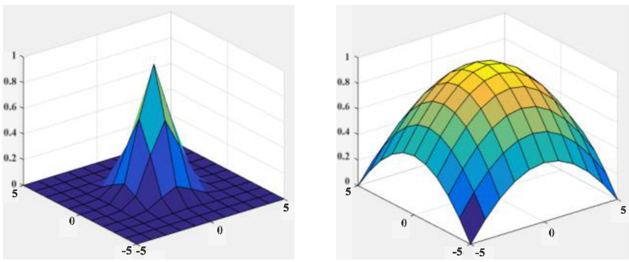

Fig. 1. LSP curves of the 5×5 spatial window with different σ.

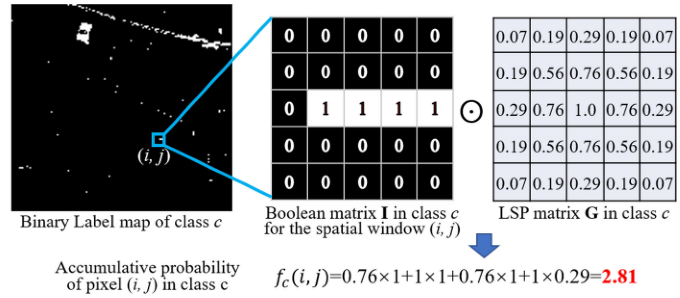

Fig. 2. Illustration of LSPF in each class c.

determines the degradation gradients of LSP. For example, in a 5×5 spatial window, both x and y range from -2 to 2 with a step interval of 1. The standard deviation σ determines the degradation gradients of LSP from the centered pixel to its nearby ones.

Considering the spatial heterogeneity of ground objects in different local windows, the σ in each spatial window can be adaptively estimated as

$$\sigma = \frac{L}{d^2}\sigma_{\max-\min} \tag{2}$$

where L is the number of pixels that have the same preobtained class label with the center pixel, and $\sigma_{\max-\min}$ is the interval of standard deviation across the whole image, which can be manually determined via cross validation. Fig. 1 illustrates the LSP curve from different choices of σ. A small σ brings about a steep LSP curve, indicating the stronger spatial heterogeneity and greater divergences between the center pixel and its neighbors.

C. Implementing the LSPF in All Classes

Furthermore, using the formulation of LSP in (1), in the spatial window centered by the pixel (i, j), the LSPF for each class c can be formulated as

$$f_c\ (i, j) = \sum \mathbf{I}_{ij}^c \odot \mathbf{G}_{ij} \tag{3}$$

where $f_c(i, j)$ is the accumulative probability of the center pixel (i, j) in class c, $\odot$ is the componentwise product (i.e., Hadamard product), $\mathbf{G}_{ij} = [g(x, y)] \in \mathbf{R}^{d\times d}$ is the LSP matrix in the (i, j)th spatial window, with x and y changing from $-(d-1)/2$ to $(d+1)/2$. $\mathbf{I}_{ij}^c = [I^c(x, y)] \in \mathbf{R}^{d\times d}$ is a Boolean matrix from the preobtained classification map. $I^c(x, y) = 1$ if the pixel (x, y) has the label c in the preobtained classification map; otherwise, $I^c(x, y) = 0$. With the LSPF, the accumulative probability vector of each pixel on each class c can be obtained. Fig. 2 illustrates the procedure of LSPF in each class c.

D. Procedure of LSPF for Hyperspectral Postclassification

Fig. 3 shows the flowchart of LSPF for refining a preobtained classification map of HSI data from SVM. The main procedure includes the following four main steps.

1) Classifying spectral signatures using an SVM classifier: With the randomly selected training samples, spectral signatures are implemented to produce the initial classification map from the SVM classifier.
2) Making binarization to the initial classification map: The initial classification map is transformed into a series of binary label maps, according to whether a pixel belongs to the class c or not. That is, in the cth binary map, the pixels have the class label c, which will be set to be 1, otherwise 0. For example, if there were 16 classes of ground objects in the image scene, the preobtained classification map can be divided into 16 layers of binary maps. In the layer of class c, each pixel would be assigned 1 or 0 according to whether its preobtained label belongs to the class c.
3) Implementing the LSPF of each class on all the pixels: Using the LSPF, for each spatial window, the accumulative probability $f_c(i, j)$ of pixel (i, j) on class c can be calculated. After that, by traversing all the classes, the accumulative probability data $\boldsymbol{F}_c\ (i, j) = [f_c(i, j)]_{c=1}^C$ of all the pixels can be obtained, which formulates a $1 \times C$ vectors on each pixel.
4) Classifying the cumulative probabilities using the regular SVM classifier: Using the regular SVM classifier and a small proportions of training pixels, the cumulative probability data of all pixels are implemented to train the SVM classifier and obtain the reclassified map of ground objects from hyperspectral data.

III. Experimental Results and Analysis

A. Hyperspectral Data

The Indian data: the data were downloaded from the website of multispectral image data analysis system at Purdue University (https://engineering.purdue.edu/∼biehl/MultiSpec/aviris_documen-tation.html). The image scene was taken by the AVIRIS sensor on June 12, 1992, that covers a part of Indiana and contains 224 bands with 145×145 pixels, and the spatial resolution and the spectral resolution are 20 m and 10 nm, respectively, and the spectral range is from 200–2400 nm. After removing the bands with severe water vapor absorption, a total of 200 bands were used in experiments. The data contain 16 types of ground objects (Corn-no till, Corn-min till, Corn, Soybeans-no till, Soybeans-min till, Soybeans-clean till, Alfalfa, Grass/pasture, Grass/tress, Grass/pasture-mowed, Hay-windrowed, Oats, Wheat, Woods, Bldg-Grass-Tree-Drives, Stone-steel towers).

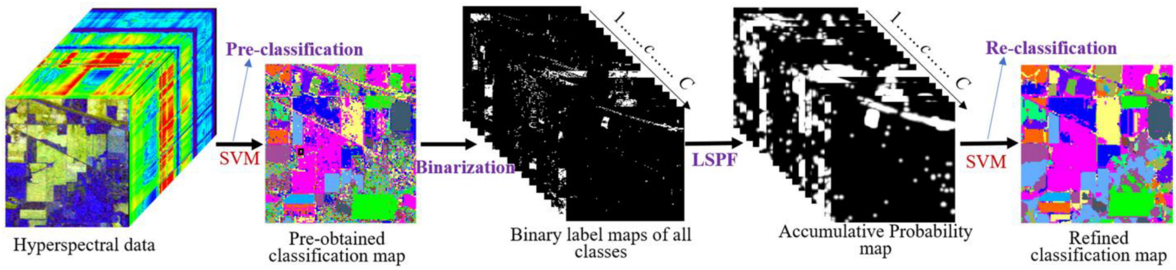

Fig. 3. Flowchart of LSPF for hyperspectral postclassification.

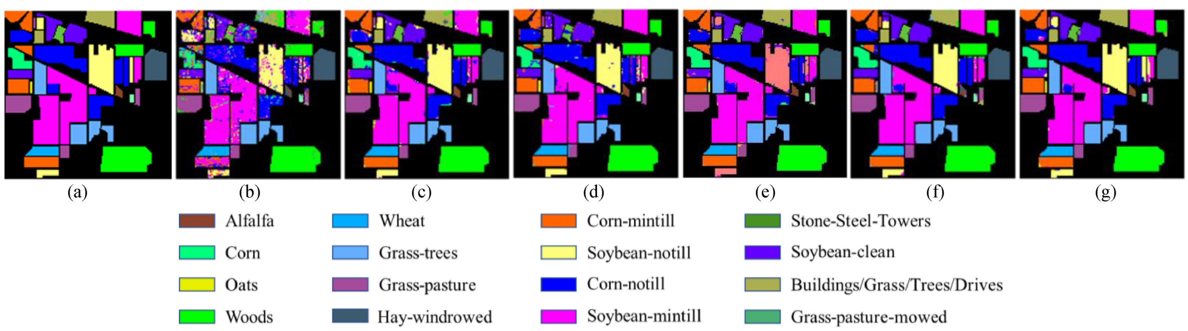

Fig. 4. Classification maps of Indian Pines dataset from different methods. (a) Ground truth. (b) SVM-SF (OA = 80.17%). (c) SLIC (OA = 95.90%). (d) EAP (OA = 94.40%). (e) SVM-CK (OA = 96.46%). (f) BF (OA = 95.14%). (g) LSPF (OA = 97.33%).

The Pavia University data: the data were downloaded from the Computational Intelligence Group from the Basque University (UPV/EHU) (http://www.ehu.es/ccwintco/index.php/Hyperspectral_Remote_Sensing_Scenes). The image was acquired by ROSIS sensors that cover the Pavia University area and contain 115 bands with 610 $\times$ 340 pixels, and the spatial resolution is 1.3 m. After removing the water vapor absorption bands, 103 bands were used. The ground objects contain nine types (Asphalt, Meadows, Metal, Gravel, Trees, Shadow, BS, Bitumen, and Bricks).

The Yellow River Estuary data: the data were downloaded from the Natural Resources Satellite Remote Sensing Cloud Service Platform (http://sasclouds.com/chinese/normal/), captured by ZY-1-02D sensor launched by China and covers the Yellow River Estuary area. The data were collected on June 28, 2019, including 166 bands with 30 m spatial resolution, and spatial size of 1147 $\times$ 1600 pixels, with a spectral range of 400–2500 nm and a spectral resolution of 20 nm. A total of 47 bands of water vapor absorption were removed, and 119 bands were finally used in the experiment. The samples were collected from the field and including 23 types of ground objects (Reed, Spartina alterniflora, Salt filter tank, Evaporation pool, Dry pond, Tamarisk, Salt marsh, Seepweed, River, Sea, Mud flat, Tidal creek, Spare farmland, Ecological pond, Locust, Fish pond, Swag, Building, Bare, Paddy fields, Crop1, Crop2, and Crop3) [see Fig. 6(a)].

B. Parameter Tuning

The SVM classifier implements with the radial basis functions (RBF) as the kernel function, and the variance parameter and the penalization factor are obtained via cross validation [36]. Overall accuracy (OA) [37], average accuracy (AA) [38], and Kappa coefficient (KC) [39] are used to quantify the classification accuracy. In the experiments, 10% labeled samples on each class of Indian Pines, Pavia University, and Yellow River Estuary dataset are randomly selected to train the SVM, and 90% labeled samples are used for testing.

C. Classification Results of LSPF Versus Other Methods

This proposed LSPF is compared with five state-of-the-art methods, including spectral characteristics-based methods: only spectral features (SF) are used for classification by SVM (SVM-SF) [40], preprocessing-based methods: extend attribute profile (EAP) [41] and simple linear iterative clustering (SLIC) [42], integrated-based methods: SVM-CK [43], and postprocessing-based methods: BF [44].

We used cross validation to select the proper parameters of various methods in this experiment. For EAP, the selection of the number of principal components and the area threshold are two important parameters, which are set to 3 and [50, 170, 360, 650, 960, 1370, 1850, 2400] in all datasets, respectively [45]. For SLIC, the size of superpixel and the selection of regularization parameters directly affect the classification performance and are set to 5 and 0.01 in the Indian Pines data, 7 and 1.5 in the Pavia University data, and 9 and 0.08 in the Yellow River Estuary data, respectively [46]. For SVM-CK, average SF and RBF functions are used to construct the composite kernel, and the patch size is set to 9 in all datasets [47]. In BF, the local spatial window size and weight for all datasets are set to 4 and 0.2, respectively [48]. For LSPF, the optimal spatial window size (d) and the

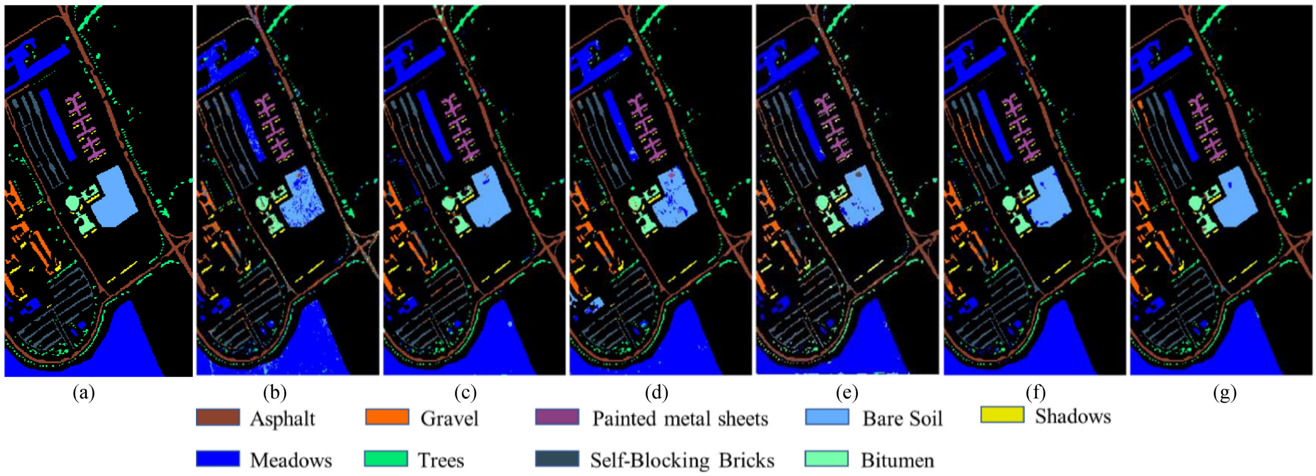

Fig. 5. Classification image of Pavia University data from different methods. (a) Ground truth. (b) SVM-SF (OA = 88.09%). (c) SLIC (OA = 93.10%). (d) EAP (OA = 94.98%). (e) SVM-CK (OA = 93.68%). (f) BF (OA = 95.50%). (g) LSPF (OA = 97.62%).

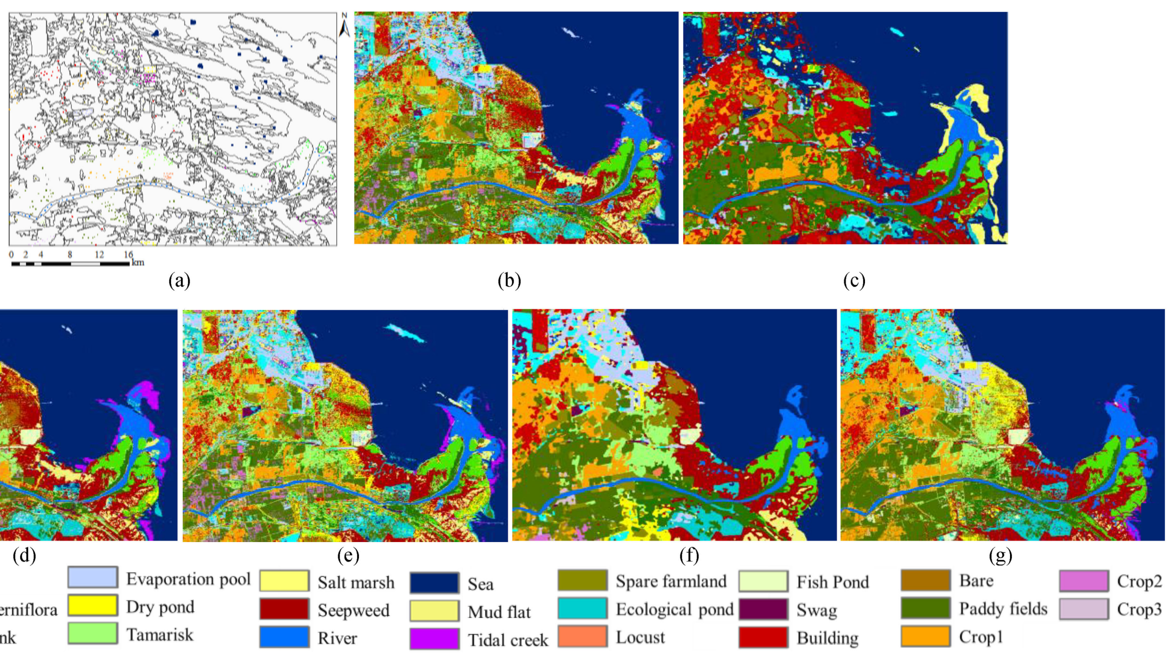

Fig. 6. Classification image of Yellow River Estuary dataset from different methods. (a) Sample distribution map. (b) SVM-SF (OA = 83.62%). (c) SLIC (OA = 72.08%). (d) EAP (OCA = 94.62%). (e) SVM-CK (OA = 86.70%). (f) BF (OA = 85.77%). (g) LSPF (OCA = 93.10%).

interval of standard deviation (σ) are 13 and 6 in all datasets, respectively.

1) Indian Pines Data: Table I presents the classification accuracy of different methods in the Indian Pines dataset. Our LSPF achieves the best classification accuracy in Corn-notill, Corn-mintill, Corn, Grass-pasture, Soybean-notill, Soybean-min, and Bldg/Grass. The accuracy of other objects is higher than 80%, and the best OA, AA, and KC are achieved, which shows that LSPF has comparative performance compared with other benchmark methods. SLIC and EAP are the second, and the classification accuracy of all ground objects is higher than 80%. SVM-CK obtains poor accuracy in Oats, and other ground objects achieve higher accuracy. BF obtains the worst classification accuracy in Grass-past-mov and Oats, and SVM-SF achieves the worst accuracy evaluation result in almost all ground objects. Moreover, Fig. 4 illustrates the classification maps. SVM-SF achieves the worst visualization effect and results in a lot of noisy labels. SLIC, EAP, and SVM-CK have poor edge classification behaviors of ground objects. For example, Corn-mintill is misclassified with Soybean-notil in SLIC, the edge of Grass-pasture is misclassified with Soybean-notil in EAP, Oats is wrongly classified as Corn-mintil in SVM-CK, and the edges of Corn-notil and Soybean-clean are misclassified with Soybean-mintil in all these methods. Compared with other

TABLE I
CLASSIFICATION ACCURACY OF INDIAN PINES DATASET FROM DIFFERENT METHODS (%)

Classes	Train	Test	SVM-SF	SLIC	EAP	SVM-CK	BF	LSPF
Alfalfa	5	41	36.10±12.72	93.17±3.18	**95.12±1.72**	90.24±9.05	90.24±18.01	91.71±4.43
Corn-notill	143	1285	77.12±2.27	94.80±2.33	86.82±1.43	96.08±1.40	93.14±1.28	**96.37±0.82**
Corn-mintill	83	747	63.67±4.58	93.44±2.73	92.40±1.15	94.95±2.73	91.75±3.27	**96.87±2.23**
Corn	24	213	52.86±10.34	91.64±1.89	90.42±3.19	96.06±3.15	97.84±3.82	**98.78±0.79**
Grass-pasture	48	435	89.70±1.92	96.55±2.37	92.74±2.64	94.87±2.58	91.72±5.14	**96.92±1.18**
Grass-trees	73	657	95.83±1.38	99.33±0.32	99.24±0.36	99.15±0.69	**99.70±0.43**	98.81±0.50
Grass-past-mov	3	25	50.40±25.86	**96.00±5.66**	90.40±10.43	90.40±10.19	33.60±43.96	94.40±10.43
Hay-windrowed	48	430	95.95±1.29	99.67±0.31	99.91±0.21	99.44±0.79	**100.00±0.00**	99.95±0.10
Oats	2	18	42.22±13.94	**94.44±3.93**	91.11±9.88	62.78±25.40	15.56±34.78	82.22±20.18
Soybean-notill	97	875	73.51±3.16	93.05±2.15	88.98±3.94	93.25±3.62	92.46±4.72	**96.05±1.40**
Soybean-min	246	2209	80.92±1.07	96.36±0.95	96.79±1.29	97.18±0.71	95.04±2.58	**96.78±1.17**
Soybean-clean	59	534	71.91±5.14	93.48±3.18	92.10±2.62	92.36±3.39	**98.20±0.90**	97.12±2.48
Wheat	21	184	98.80±0.71	98.59±2.29	**99.46±0.38**	99.02±1.33	99.46±0.00	98.70±0.73
Woods	127	1138	94.55±2.37	99.47±0.25	**99.82±0.09**	98.60±1.61	99.58±0.38	98.89±0.79
Bldg/Grass	39	347	59.60±8.49	93.60±2.85	97.87±1.05	95.79±2.63	91.76±8.01	**98.90±0.94**
Towers	9	84	80.00±4.41	85.24±6.87	91.67±9.82	92.62±5.01	**99.76±0.53**	95.24±3.26
	OA		80.17±0.48	95.90±0.53	94.40±0.38	96.46±0.73	95.14±0.86	**97.33±0.48**
	AA		72.70±0.82	94.93±1.06	94.05±1.77	93.30±2.22	86.86±2.53	**96.11±1.86**
	KC		77.32±0.56	95.32±0.61	93.61±0.44	95.96±0.84	76.39±1.31	**96.96±0.54**

TABLE II
CLASSIFICATION ACCURACY OF PAVIA UNIVERSITY DATA FROM DIFFERENT METHODS (%)

Classes	Train	Test	SVM-SF	SLIC	EAP	SVM-CK	BF	LSPF
Asphalt	66	6565	87.01±1.59	91.37±1.19	**98.50±0.86**	94.17±2.22	97.17±1.32	96.97±0.91
Meadows	186	18463	96.05±1.33	99.48±0.38	97.86±1.28	98.49±0.76	**99.70±0.26**	99.46±0.41
Gravel	21	2078	53.63±7.26	72.95±5.97	83.32±4.35	82.16±5.18	74.55±6.26	**90.07±5.11**
Trees	31	3033	88.39±2.15	83.06±6.09	92.71±3.64	89.06±5.08	90.61±2.43	**92.43±3.34**
Metal sheets	13	1332	98.47±0.70	**99.14±0.59**	99.08±0.56	99.89±0.22	94.10±11.99	98.7±1.06
Bare Soil	50	4979	73.95±4.90	96.52±0.85	83.82±6.00	93.26±3.11	93.64±4.66	**99.68±0.45**
Bitumen	13	1317	77.42±8.65	82.63±7.33	92.53±8.53	89.45±4.52	83.46±17.01	**94.31±5.98**
Bricks	37	3645	85.75±4.18	83.23±1.21	96.51±1.33	82.48±2.51	95.93±1.80	**96.01±1.05**
Shadows	9	938	**98.87±1.42**	83.26±7.04	97.93±2.09	80.07±6.70	90.62±9.30	97.57±1.60
	OA		88.09±0.34	93.10±0.69	94.98±0.37	93.68±0.43	95.50±0.49	**97.62±0.23**
	AA		84.39±1.45	87.96±1.24	93.59±0.43	89.89±0.83	91.09±1.61	**96.14±0.55**
	KC		84.09±0.54	90.82±0.93	93.31±0.51	91.59±0.55	83.17±1.23	**96.84±0.30**

methods, the visualization behavior of BF is better, and there is a small number of errors at the edge of Soybean-mintil. LSPF achieves the best visualization results of all.

2) Pavia University Data: Table II presents the quantitative evaluation results of different methods on the Pavia University data. Our LSPF is still superior to all benchmark methods and has the best classification accuracy in Corn-notill, Corn-mintill, Corn, Grass-pasture, Soybean-notill, Soybean-min, and Bldg/Grass; the classification accuracy of other ground objects is higher than 90%, and the best OA, AA, and KC are obtained. SLIC and EAP are raking the second, their classification accuracies of all ground objects are higher than 85%, and OA, AA, and KC are higher than 90%. SVM-CK obtains lower accuracy in Oats. But the classification accuracy of other ground objects, OA, AA, and KC are higher than 90%, which still has comparative performance. BF obtains the worst classification accuracy in Grass-past-mov and Oats, SVM-SF has the worst classification behaviors, and almost all ground objects have the lowest classification accuracy. The classification results of the Pavia University dataset are shown in Fig. 5; SLIC and BF achieve better visualization results. However, there are still obvious misclassifications between Bare soil and Meadows, and Gravel and self-blocking bricks. EPA and SVM-CK are the second, and there are obvious noise spots in Bare soil. SVM-SF has the worst visualization results and many noise spots exist in Bare Soil and Meadows. Compared with these benchmark methods, LSPF obtains the best visualization results.

3) Yellow River Estuary Data: Fig. 6 shows the classification results of the Yellow River Estuary data. SLIC and BF have better visualization results. However, the serious misclassifications always exist. SVM-SF and SVM-CK have poor visualization effects and a lot of noise spots. Compared with other benchmark methods, EAP obtains a better visualization effect, and our method is the best. The accuracy evaluation results of various methods are also shown in Table III. SLIC has the lowest classification accuracy in almost all features and the worst OA, AA, and KC. SVM-SF, SVM-CK, and BF are followed, except for Reed, Tamarisk, Mud flat, Tidal creek, Locust, Fish pond, Swag, Crop1, and Crop2; the classification accuracy of other features and AA are higher than 80%, and OA and KC are greater than 90%. EPA is the best among all benchmark methods. Except Tidal Creek, the classification accuracy of other ground objects is higher than 85%, and OA, AA, and KC are higher than 90%. Our method achieves the best classification results compared with these benchmark methods and obtains the highest classification accuracy in Spartina alterniflora, Evaporation pool, Tamarisk, Seepweed, River, Sea, Spare farmland, Ecological pond, Locust, Fish pond, Bare, Paddy

TABLE III
CLASSIFICATION ACCURACY OF YELLOW RIVER ESTUARY DATA FROM DIFFERENT METHODS (%)

Classes	Train	Test	SVM-SF	SLIC	EAP	SVM-CK	BF	LSPF
Reed	31	279	59.93±6.12	71.90±5.79	**91.33±3.84**	64.09±5.71	65.81±6.86	90.82±2.86
Spartina alterniflora	19	168	95.00±4.66	88.45±3.94	99.29±0.95	92.5±4.86	94.76±4.68	**99.52±0.5**
Salt filter tank	25	222	96.76±3.9	79.20±0.92	97.48±1.29	**97.93±1.48**	97.03±6.65	96.04±5.17
Evaporation pool	30	270	96.44±2.52	74.22±5.39	96.44±1.82	95.26±3.46	91.19±6.02	**98.66±1.61**
Dry pond	14	126	94.13±2.42	94.13±4.22	97.14±3.50	97.30±3.35	**98.10±2.84**	94.76±3.05
Tamarisk	13	114	72.63±6.49	79.82±2.06	85.61±7.66	87.54±7.86	71.75±3.36	**89.12±5.29**
Salt marsh	31	275	97.31±1.05	87.93±7.37	**100±0**	99.27±1.06	98.69±1.81	99.35±0.30
Seepweed	22	196	98.36±2.03	91.48±6.84	98.769±.54	96.62±2.53	99.59±0.92	**100±0**
River	58	526	**100±0**	98.97±0.71	**100±0**	**100±0**	**100±0**	**100±0**
Sea	469	4225	99.97±0.052	97.83±1.53	99.89±0.09	99.87±0.13	**100±0.01**	**100±0**
Mud flat	3	13	67.69±6.44	35.38±6.9	**87.69±5.07**	60±20.64	69.23±0	75.38±3.76
Tidal creek	7	60	48±9.08	40.67±9.90	**76.33±9.45**	51±18.13	57.33±23.00	55.33±2.55
Spare farmland	46	413	96.76±1.48	85.13±4.63	98.50±1.74	96.37±2.57	97.63±1.77	**99.23±0.86**
Ecological pond	31	279	88.67±5.03	76.92±6.46	95.99±2.6	90.47±2.19	92.33±5.33	**97.99±2.19**
Locust	11	100	76.4±10.92	30.6±41.50	96±2.10	86±5.52	91.8±5.22	**98.2±1.10**
Fish pond	12	112	76.61±5.63	80.89±0.49	93.57±4.80	69.11±6.69	70.36±4.21	**97.5±2.98**
Swag	13	115	68.52±11.64	25.91±8.35	**93.22±7.75**	67.13±7.13	52.35±12.83	79.48±0.19
Building	40	358	88.21±4.49	74.80±7.31	**98.04±0.91**	91.96±0.95	95.47±2.58	94.02±6.33
Bare	9	78	82.56±9.36	51.03±8.67	97.95±0.63	90.77±0.43	93.85±6.75	**99.74±0.57**
Paddy fields.	51	457	92.70±3.330	85.89±0.54	98.55±0.69	93.85±4.30	93.98±1.69	**98.90±0.71**
Crop1	33	299	74.92±3.79	69.23±3.76	86.69±2.48	84.75±4.61	79.93±3.42	**96.45±2.58**
Crop2	7	64	68±14.69	61.00±9.95	89.67±7.77	89±4.50	81.33±11.14	**91.33±3.91**
Crop3	10	93	83.66±3.98	76.34±7.86	**94.19±7.09**	93.33±5.66	89.25±4.30	89.46±4.65
OA			93.74±0.36	87.90±.760	96.87±0.25	94.93±0.32	94.75±0.406	**97.97±0.56**
AA			83.62±0.87	72.08±2.15	**94.62±1.03**	86.70±1.05	85.77±1.27	93.10±1.89
KC			91.67±0.477	83.86±2.33	97.01±0.33	93.25±0.42	93.01±0.56	**97.41±0.74**

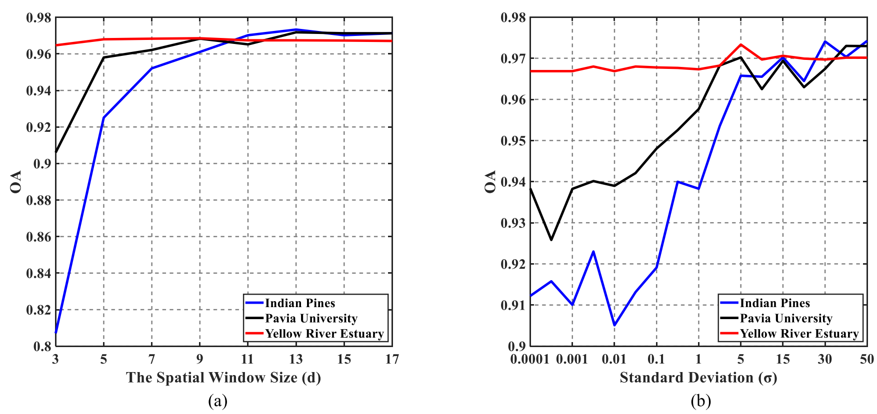

Fig. 7. Impacts of (a) spatial window size d and (b) standard deviation σ in LSPF.

fields, Crop1, Crop2, and OA, AA, and KC, which are higher than 90%.

D. Impacts From Two Key Parameters in LSPF

In this section, we investigate the influences of tradeoff parameters, d and σ, on the performance of the proposed method. The results on Indian Pines, Pavia University, and Yellow River Estuary data are shown in Fig. 7, where d varies from 3 to 17 with step 2 in power. It can be observed that except for Yellow River Estuary data, superior indices are produced and the variations of all evaluation indices are obvious when d is from 3 to 11, and the changing trends are flat for a larger d. The OA increases rapidly first and then becomes flatten with the increasing d. Considering the overall results, we recommend d to be over 10 in realistic applications.

Moreover, we set the range of standard deviation within [0.0001, 0.0005, 0.001, 0.005, 0.01, 0.05, 0.1, 0.5, 1, 2, 5, 10, 15, 20, 30, 40, 50] to investigate the optimal σ. Superior behaviors are obvious in Indian Pines and Pavia University dataset when σ is very large, but the change is small in the Yellow River Estuary dataset. Although there are fluctuations, the overall trend increases with the increase of σ, the fluctuation gradually decreases, and the curve tends to be flat when σ reaches 5. Therefore, a moderate σ around 6 is recommended to be implemented in realistic datasets.

IV. CONCLUSION

In this article, a novel LSPF postprocessing-based method was proposed to improve the classification accuracy of hyperspectral image. The LSPF implements the LSP into all neighboring pixels within the same spatial window and estimates the cumulative probability of all pixels in each class to refine its preobtained classification map. The experimental results on three hyperspectral datasets demonstrate that the LSPF effectively improves the prior label information and achieves the best classification accuracy compared with the other five state-of-the-art methods. Particularly, it could promote about 10% of AA in the regular SVM classifications. In realistic applications, a moderate spatial window over 10 and a moderate standard deviation around five are recommended to use for guaranteeing good performance of LSPF in hyperspectral postclassification.

REFERENCES

[1] Y.-N. Liu *et al.*, "The advanced hyperspectral imager: Aboard China's GaoFen-5 satellite," *IEEE Geosci. Remote Sens. Mag.*, vol. 7, no. 4, pp. 23–32, Dec. 2019.

[2] W. Sun, G. Yang, J. Peng, and Q. Du, "Lateral-sliceu sparse tensor robust principal component analysis for hyperspectral image classification," *IEEE Geosci. Remote Sens. Lett.*, vol. 17, no. 1, pp. 107–111, Jan. 2020.

[3] Z. Zhong, J. Li, Z. Luo, and M. Chapman, "Spectral–spatial residual network for hyperspectral image classification: A 3-D deep learning framework," *IEEE Trans. Geosci. Remote Sens.*, vol. 56, no. 2, pp. 847–858, Feb. 2018.

[4] M. Imani and H. Ghassemian, "An overview on spectral and spatial information fusion for hyperspectral image classification: Current trends and challenges," *Inf. Fusion*, vol. 59, no. 18, pp. 59–83, 2020.

[5] J. Peng, W. Sun, and Q. Du, "Self-paced joint sparse representation for the classification of hyperspectral images," *IEEE Trans. Geosci. Remote Sens.*, vol. 57, no. 2, pp. 1183–1194, Feb. 2019.

[6] X. Kang, X. Xiang, S. Li, and J. A. Benediktsson, "PCA-based edge-preserving features for hyperspectral image classification," *IEEE Trans. Geosci. Remote Sens.*, vol. 55, no. 12, pp. 7140–7151, Dec. 2017.

[7] Q. Wang, X. He, and X. Li, "Locality and structure regularized low rank representation for hyperspectral image classification," *IEEE Trans. Geosci. Remote Sens.*, vol. 57, no. 2, pp. 911–923, Feb. 2019.

[8] Q. Gao, S. Lim, and X. Jia, "Spectral–spatial hyperspectral image classification using a multiscale conservative smoothing scheme and adaptive sparse representation," *IEEE Trans. Geosci. Remote Sens.*, vol. 57, no. 10, pp. 7718–7730, Oct. 2019.

[9] P. Ghamisi, J. Plaza, Y. Chen, J. Li, and A. J. Plaza, "Advanced spectral classifiers for hyperspectral images: A review," *IEEE Geosci. Remote Sens. Mag.*, vol. 5, no. 1, pp. 8–32, Mar. 2017.

[10] L. He, J. Li, C. Liu, and S. Li, "Recent advances on spectral–spatial hyperspectral image classification: An overview and new guidelines," *IEEE Trans. Geosci. Remote Sens.*, vol. 56, no. 3, pp. 1579–1597, Mar. 2018.

[11] F. Zhou, R. Hang, Q. Liu, and X. Yuan, "Hyperspectral image classification using spectral-spatial LSTMs," *Neurocomputing*, vol. 328, no. 12, pp. 39–47, 2019.

[12] J. Jiang, J. Ma, Z. Wang, C. Chen, and X. Liu, "Hyperspectral image classification in the presence of noisy labels," *IEEE Trans. Geosci. Remote Sens.*, vol. 57, no. 2, pp. 851–865, Feb. 2019.

[13] Y. Gu, J. Chanussot, X. Jia, and J. A. Benediktsson, "Multiple kernel learning for hyperspectral image classification: A review," *IEEE Trans. Geosci. Remote Sens.*, vol. 55, no. 11, pp. 6547–6565, Nov. 2017.

[14] F. Luo, L. Zhang, X. Zhou, T. Guo, Y. Cheng, and T. Yin, "Sparse-adaptive hypergraph discriminant analysis for hyperspectral image classification," *IEEE Geosci. Remote Sens. Lett.*, vol. 17, no. 6, pp. 1082–1086, Jun. 2020.

[15] P. Duan, X. Kang, S. Li, P. Ghamisi, and J. A. Benediktsson, "Fusion of multiple edge-preserving operations for hyperspectral image classification," *IEEE Trans. Geosci. Remote Sens.*, vol. 57, no. 12, pp. 10336–10349, Dec. 2019.

[16] S. Jia, L. Shen, J. Zhu, and Q. Li, "A 3-D Gabor phase-based coding and matching framework for hyperspectral imagery classification," *IEEE Trans. Cybern.*, vol. 48, no. 4, pp. 1176–1188, Apr. 2018.

[17] Y. Gu, T. Liu, X. Jia, J. A. Benediktsson, and J. Chanussot, "Nonlinear multiple kernel learning with multiple-structure-element extended morphological profiles for hyperspectral image classification," *IEEE Trans. Geosci. Remote Sens.*, vol. 54, no. 6, pp. 3235–3247, Jun. 2016.

[18] P. Ghamisi, R. Souza, J. A. Benediktsson, L. Rittner, R. Lotufo, and X. X. Zhu, "Hyperspectral data classification using extended extinction profiles," *IEEE Geosci. Remote Sens. Lett.*, vol. 13, no. 11, pp. 1641–1645, Nov. 2016.

[19] W. Liao, M. Dalla Mura, J. Chanussot, R. Bellens, and W. Philips, "Morphological attribute profiles with partial reconstruction," *IEEE Trans. Geosci. Remote Sens.*, vol. 54, no. 3, pp. 1738–1756, Mar. 2016.

[20] X. Huang, X. Han, L. Zhang, J. Gong, W. Liao, and J. A. Benediktsson, "Generalized differential morphological profiles for remote sensing image classification," *IEEE J. Sel. Topics Appl. Earth Observ. Remote Sens.*, vol. 9, no. 4, pp. 1736–1751, Apr. 2016.

[21] P. Duan, X. Kang, S. Li, and P. Ghamisi, "Noise-robust hyperspectral image classification via multi-scale total variation," *IEEE J. Sel. Topics Appl. Earth Observ. Remote Sens.*, vol. 12, no. 6, pp. 1948–1962, Jun. 2019.

[22] L. Sun *et al.*, "Low rank component induced spatial-spectral kernel method for hyperspectral image classification," *IEEE Trans. Circuits Syst. Video Technol.*, vol. 30, no. 10, pp. 3829–3842, Oct. 2020.

[23] G. Camps-Valls, L. Gomez-Chova, J. Muñoz-Marí, J. Vila-Francés, and J. Calpe-Maravilla, "Composite kernels for hyperspectral image classification," *IEEE Geosci. Remote Sens. Lett.*, vol. 3, no. 1, pp. 93–97, Jan. 2006.

[24] J. Peng and Q. Du, "Robust joint sparse representation based on maximum correntropy criterion for hyperspectral image classification," *IEEE Trans. Geosci. Remote Sens.*, vol. 55, no. 12, pp. 7152–7164, Dec. 2017.

[25] S. Jia, X. Zhang, and Q. Li, "Spectral–spatial hyperspectral image classification using $l_{1/2}$ regularized low-rank representation and sparse representation-based graph cuts," *IEEE J. Sel. Topics Appl. Earth Observ. Remote Sens.*, vol. 8, no. 6, pp. 2473–2484, Jun. 2015.

[26] Z. Wang, B. Du, L. Zhang, Liangpei Zhang, and X. Jia, "A novel semisupervised active-learning algorithm for hyperspectral image classification," *IEEE Trans. Geosci. Remote Sens.*, vol. 55, no. 6, pp. 3071–3083, Jun. 2017.

[27] J. Liu, Z. Wu, J. Li, A. Plaza, and Y. Yuan, "Probabilistic-kernel collaborative representation for spatial–spectral hyperspectral image classification," *IEEE Trans. Geosci. Remote Sens.*, vol. 54, no. 4, pp. 2371–2384, Apr. 2016.

[28] X. Kang, S. Li, and J. A. Benediktsson, "Spectral–spatial hyperspectral image classification with edge-preserving filtering," *IEEE Trans. Geosci. Remote Sens.*, vol. 52, no. 5, pp. 2666–2677, May 2014.

[29] J. Li, J. M. Bioucas-Dias, and A. Plaza, "Spectral–spatial hyperspectral image segmentation using subspace multinomial logistic regression and Markov random fields," *IEEE Trans. Geosci. Remote Sens.*, vol. 50, no. 3, pp. 809–823, Mar. 2012.

[30] L. Fang, C. Wang, S. Li, and J. A. Benediktsson, "Hyperspectral image classification via multiple-feature-based adaptive sparse representation," *IEEE Trans. Instrum. Meas.*, vol. 66, no. 7, pp. 1646–1657, Jul. 2017.

[31] B. Tu, X. Zhang, X. Kang, J. Wang, and J. A. Benediktsson, "Spatial density peak clustering for hyperspectral image classification with noisy labels," *IEEE Trans. Geosci. Remote Sens.*, vol. 57, no. 7, pp. 5085–5097, Jul. 2019.

[32] J. Xia, P. Ghamisi, N. Yokoya, and A. Iwasaki, "Random forest ensembles and extended multiextinction profiles for hyperspectral image classification," *IEEE Trans. Geosci. Remote Sens.*, vol. 56, no. 1, pp. 202–216, Jan. 2018.

[33] R. Kemker and C. Kanan, "Self-taught feature learning for hyperspectral image classification," *IEEE Trans. Geosci. Remote Sens.*, vol. 55, no. 5, pp. 2693–2705, May 2017.

[34] T. Dundar and T. Ince, "Sparse representation-based hyperspectral image classification using multiscale superpixels and guided filter," *IEEE Geosci. Remote Sens. Lett.*, vol. 16, no. 2, pp. 246–250, Feb. 2019.

[35] S. Jia, X. Deng, J. Zhu, M. Xu, J. Zhou, and X. Jia, "Collaborative representation-based multiscale superpixel fusion for hyperspectral image classification," *IEEE Trans. Geosci. Remote Sens.*, vol. 57, no. 10, pp. 7770–7784, Oct. 2019.

[36] L. Xie, G. Li, M. Xiao, L. Peng, and Q. Chen, "Hyperspectral image classification using discrete space model and support vector machines," *IEEE Geosci. Remote Sens. Lett.*, vol. 14, no. 3, pp. 374–378, Mar. 2017.

[37] C. J. Della Porta, A. A. Bekit, B. H. Lampe, and C.-I. Chang, "Hyperspectral image classification via compressive sensing," *IEEE Trans. Geosci. Remote Sens.*, vol. 57, no. 10, pp. 8290–8303, Oct. 2019.

[38] Y. Zhang, G. Cao, X. Li, and B. Wang, "Cascaded random forest for hyperspectral image classification," *IEEE J. Sel. Topics Appl. Earth Observ. Remote Sens.*, vol. 11, no. 4, pp. 1082–1094, Apr. 2018.

[39] S. Zhong *et al.*, "Class feature weighted hyperspectral image classification," *IEEE J. Sel. Topics Appl. Earth Observ. Remote Sens.*, vol. 12, no. 12, pp. 4728–4745, Dec. 2019.

[40] U. Maulik and D. Chakraborty, "Remote sensing image classification: A survey of support-vector-machine-based advanced techniques," *IEEE Geosci. Remote Sens. Mag.*, vol. 5, no. 1, pp. 33–52, Mar. 2017.

[41] M. Liu, F. Cao, Z. Yang, X. Hong, and Y. Huang, “Hyperspectral image denoising and classification using multi-scale weighted EMAPs and extreme learning machine,” *Electronics*, vol. 9, no. 12, 2020, Art. no. 2137.

[42] Y. Zhang, K. Liu, Y. Dong, K. Wu, and X. Hu, “Semisupervised classification based on SLIC segmentation for hyperspectral image,” *IEEE Geosci. Remote Sens. Lett.*, vol. 17, no. 8, pp. 1440–1444, Aug. 2020.

[43] X. Zhang, Y. Liang, C. Li, N. Huyan, L. Jiao, and H. Zhou, “Recursive autoencoders-based unsupervised feature learning for hyperspectral image classification,” *IEEE Geosci. Remote Sens. Lett.*, vol. 14, no. 11, pp. 1928–1932, Nov. 2017.

[44] B. Tu, X. Zhang, J. Wang, G. Zhang, and X. Ou, “Spectral–spatial hyperspectral image classification via non-local means filtering feature extraction,” *Sens. Imag.*, vol. 19, no. 1, 2018, Art. no. 11.

[45] L. Liu, W. Huang, and C. Wang, “Hyperspectral image classification with kernel-based least-squares support vector machines in sum space,” *IEEE J. Sel. Topics Appl. Earth Observ. Remote Sens.*, vol. 11, no. 4, pp. 1144–1157, Aug. 2018.

[46] B. Zu *et al.*, “SLIC superpixel-based $l_{2,1}$-norm robust principal component analysis for hyperspectral image classification,” *Sensors*, vol. 19, no. 3, 2019, Art. no. 479.

[47] D. Li, X. Wang, and Y. Cheng, “Spatial-spectral neighbour graph for dimensionality reduction of hyperspectral image classification,” *Int. J. Remote Sens.*, vol. 40, no. 11, pp. 4361–4383, 2019.

[48] Z. Chen, J. Jiang, C. Zhou, X. Jiang, S. Fu, and C. Zhihua, “Trilateral smooth filtering for hyperspectral image feature extraction,” *IEEE Geosci. Remote Sens. Lett.*, vol. 16, no. 5, pp. 781–785, May 2019.

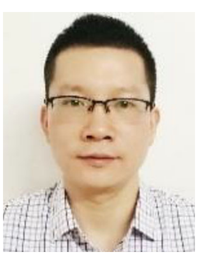

Weiwei Sun (Senior Member, IEEE) received the B.S. degree in surveying and mapping and the Ph.D. degree in cartography and geographic information engineering from Tongji University, Shanghai, China, in 2007 and 2013, respectively.

From 2011 to 2012, he was with the Department of Applied Mathematics, University of Maryland, College Park, working as a Visiting Scholar with the famous Professor John Benedetto to study on the dimensionality reduction of hyperspectral image. From 2014 to 2016, he was with the State Key Laboratory for Information Engineering in Surveying, Mapping, and Remote Sensing, Wuhan University, working as a Postdoctor to study intelligent processing in hyperspectral imagery. From 2017 to 2018, he was a Visiting Scholar with the Department of Electrical and Computer Engineering, Mississippi State University. He is currently a Full Professor with Ningbo University, Ningbo, China. He has authored or coauthored more than 70 journal papers and his current research interests include hyperspectral image processing with manifold learning, anomaly detection, and target recognition of remote sensing imagery using compressive sensing.

Gang Yang (Member, IEEE) received the M.S. degree in geographical information system from the Hunan University of Science and Technology, Xiangtan, China, in 2012, and the Ph.D. degree in cartography and geography information system from the School of Resource and Environmental Sciences, Wuhan University, Wuhan, China, in 2016.

He is currently an Assistant Professor with Ningbo University, Ningbo, China. His research interests include missing information reconstruction of remote sensing image, cloud removal of remote sensing image, and remote sensing time-series products temporal reconstruction.

Kai Ren received the B.S. degree in humanistic geography and urban–rural planning from Shanxi Normal University, Xi’an, China, in 2018. He is currently working toward the master’s degree with Ningbo University, Ningbo, China.

His research interests include remote sensing data fusion and data analysis.

Jiangtao Peng (Senior Member, IEEE) received the B.S. degree in information and computing sciences and M.S. degree in applied mathematics from Hubei University, Wuhan, China, in 2005 and 2008, respectively, and the Ph.D. degree in pattern recognition and intelligent systems from the Institute of Automation, Chinese Academy of Sciences, Beijing, China, in 2011.

He is currently a Professor with the Faculty of Mathematics and Statistics, Hubei University. His research interests include machine learning and hyperspectral image processing.

Chiru Ge (Student Member, IEEE) received the B.E. degree in communication engineering from Shandong Normal University, Jinan, China, in 2012. He is currently working toward the Ph.D. degree in communication and information systems from Xidian University, Xi’an, China.

From 2017 to 2018, he was with the Department of Electrical and Computer Engineering, Mississippi State University, Starkville, MS, USA, as a Visiting Scholar with Professor Qian Du to study on hyperspectral and LiDAR image fusion. His research interests include hyperspectral remote sensing image analysis and processing, hyperspectral, and LiDAR image fusion.

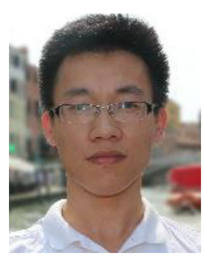

Xiangchao Meng (Member, IEEE) received the B.S. degree in geographic information system from the Shandong University of Science and Technology, Qingdao, China, in 2012, and the Ph.D. degree in cartography and geography information system from Wuhan University, Wuhan, China, in 2017.

He is currently an Assistant Professor with the Faculty of Electrical Engineering and Computer Science, Ningbo University, Ningbo, China. His research interests include machine learning, multisource data fusion and applications, and quality evaluation.

Qian Du (Fellow, IEEE) received the Ph.D. degree in electrical engineering from the University of Maryland-Baltimore County, Baltimore, MD, USA, in 2000.

She is currently a Bobby Shackouls Professor with the Department of Electrical and Computer Engineering, Mississippi State University, Starkville, MS, USA. Her research interests include hyperspectral remote sensing image analysis and applications, pattern classification, data compression, and neural networks.

Dr. Du is a Fellow of the SPIE-International Society for Optics and Photonics. She was a recipient of the 2010 Best Reviewer Award from the IEEE Geoscience and Remote Sensing Society. She was a Co-Chair of the Data Fusion Technical Committee of the IEEE GRSS from 2009 to 2013, the Chair of the Remote Sensing and Mapping Technical Committee of the International Association for Pattern Recognition from 2010 to 2014, and the General Chair of the fourth IEEE GRSS Workshop on Hyperspectral Image and Signal Processing: Evolution in Remote Sensing held at Shanghai, China, in 2012. She was an Associate Editor for the *IEEE Journal of Selected Topics in Applied Earth Observations and Remote Sensing* (JSTARS), the *Journal of Applied Remote Sensing*, and the *IEEE Signal Processing Letters*. Since 2016, she has been the Editor-in-Chief for the *IEEE JSTARS*.